Micron 77 (2015) 57–65

Contents lists available at ScienceDirect

Micron

journal homepage: www.elsevier.com/locate/micron

Gentle quantitative measurement of helium density in nanobubbles in silicon by spectrum imaging

Kévin Alix[a], Marie-Laure David[a,*], Guillaume Lucas[b], Duncan T.L. Alexander[b], Frédéric Pailloux[a], Cécile Hébert[b], Laurent Pizzagalli[a]

[a] Institut Pprime, UPR3346 CNRS-Université de Poitiers, 86962 Futuroscope-Chasseneuil, France
[b] CIME, EPFL-SB-CIME-GE, CH-1015 Lausanne, Switzerland

ARTICLE INFO

Article history:
Received 4 March 2015
Received in revised form 19 May 2015
Accepted 19 May 2015
Available online 27 May 2015

Keywords:
EELS
EFTEM
Spectrum imaging
Helium bubbles
Implantation

ABSTRACT

We propose an original method for the determination of the physical properties of nanometer sized helium bubbles using spectrum imaging in an energy-filtered transmission electron microscope. Helium bubbles synthesized by high fluence implantation and thermal annealing in silicon are investigated. The acquisition parameters are determined to optimize both signal/noise ratio and time. The limitations to the extent of observable areas on a typical sample are explained. The necessary data correction and helium K-edge position measurement procedures are detailed and the accuracy of the method is discussed. Finally helium density maps are obtained and discussed.

© 2015 Elsevier Ltd. All rights reserved.

1. Introduction

When introduced in high concentration in materials, helium tends to agglomerate and form nanometer-sized bubbles (Donnelly and Evans, 1991; Raineri and Saggio, 2000; Cerofolini et al., 2000). For instance, helium bubbles can be synthesized using ion implantation. Specific implantation and annealing parameters in a given material lead to reproducible results, which allow the study of those bubbles and their contents in a statistical way. Helium bubbles can also be obtained as a by-product of nuclear reactions, as charged α particles are emitted and eventually impact either the walls, or the fuel inside a nuclear reactor (Guilbert et al., 2003). Helium bubbles usually have detrimental effects on the materials in which they are embedded; in the nuclear-energy context, embrittlement is an important one (Trinkaus and Singh, 2003). But in the microelectronic field they can have several applications such as impurity gettering (Petersen et al., 1997) and production of silicon on insulator (SOI) wafers using the layer splitting by ion cutting process (Bruel, 1995; Agarwal et al., 1998). Moreover, low energy helium plasma treatments have recently received considerable interest for nanostructuration of surfaces with applications in domains of energy conversion and storage devices, by both bottom-up (Godinho et al., 2013) or top-down approaches (Kajita et al., 2013; Iyyakkunnel et al., 2014). In particular, nanopores in amorphous silicon coatings produced using such methods have been revealed to contain a high helium density (Schierholz et al., 2015). In any case, in order to better predict these effects and their properties, and to control them, extensive study of bubble formation and evolution mechanisms under annealing or irradiation is a prerequisite.

The important parameters required to validate growth models are the size, morphology, and helium density of the bubbles. The helium density can then be converted to pressure in the bubbles through an appropriate equation of state (Trinkaus, 1983; David et al., 2014). Conventional transmission electron microscopy (TEM) can be used to obtain the size and morphology of the bubbles, but the determination of their helium density requires a more complex approach. One such approach is the measurement of diffraction contrast features in TEM micrographs (Tillmann et al., 2004). However it is not well adapted to the study of spherical nano-bubbles. Indeed, the strain field in that case leads to more complex contrasts in dark field or bright field imaging than that which is observed for platelet defects, and these contrasts are tricky to be used for quantification. Another powerful approach is spatially-resolved electron energy-loss spectroscopy (EELS) using scanning TEM (STEM). This method has been used for bubbles embedded in various matrices (Schierholz et al., 2015; David et al., 2014, 2011; Manzke et al., 1982; Jaeger et al., 1982, 1983; McGibbon, 1991; Walsh et al.,

* Corresponding author.
E-mail address: marie-laure.david@univ-poitiers.fr (M.-L. David).

http://dx.doi.org/10.1016/j.micron.2015.05.011
0968-4328/© 2015 Elsevier Ltd. All rights reserved.

2000; Taverna et al., 2008; Frechard et al., 2009). However, we have demonstrated that it can show an adverse effect when helium bubbles are embedded in silicon or germanium (David et al., 2014, 2011), as it can trigger helium detrapping upon electron irradiation from the probe. This has recently been observed in the case of helium nanopores in silicon as well (Schierholz et al., 2015). While this process is slow enough for a one-time measurement, it effectively renders repetition of the same measurement unfeasible. This hinders the application of STEM-EELS in a conventional TEM/STEM for He density measurements during *in situ* experiments, as those require several scans on each analyzed bubble upon, for instance, annealing or irradiation.

A possible alternative to STEM-EELS is spectrum imaging in an energy-filtered TEM (EFTEM-SI), which is based on the acquisition of a series of energy-filtered images at different energy-losses (Jeanguillaume and Colliex, 1989; Lavergne et al., 1992; Verbeeck et al., 2004).

EFTEM-SI has been shown to be a powerful tool to gather information in the low loss part of the spectrum, for example for plasmon imaging (Eggeman et al., 2007; Schaffer et al., 2009, 2010; Nelayah et al., 2009; Sigle et al., 2010) for instance. Moreover, with the EFTEM approach, the illumination conditions are drastically different from STEM-EELS, in terms of current density in particular, as a parallel beam is used instead of a focused probe. This may reduce some effects of electron beam damage, as was recently observed in $LiFePO_4$ (Sugar et al., 2014) and also in polymers (Allen et al., 2011). Our hypothesis was that helium detrapping under the electron beam would be negligible with an EFTEM-SI approach. EFTEM-SI is further useful for the acquisition of maps over large fields of view using relatively short acquisition times, and is hence more suitable than STEM-EELS based approaches when observing a large amount of bubbles. It is thus a potentially valuable technique to investigate the physical properties of helium bubbles in a statistical way.

Here, we describe and validate a method using EFTEM-SI for the determination of the helium density in nano-bubbles in silicon.

2. Sample preparation

The samples used for this study were implanted with 50 keV helium ions at a fluence of $7.5{\cdot}10^{16}$ at.cm^{-2}. The implantations were performed on mono-crystalline p-type Si wafers. The samples were then annealed at temperatures of 500 or 700 °C, chosen for their known results in terms of microstructure, and expected different characteristics of the helium bubbles (size, morphology, He density, pressure) (David et al., 2011).

After implantation and annealing, the Si wafers were mechanically cleaved, wire-sawed and glued face-to-face, in order to obtain cross-sections of the implanted material. The samples were then thinned by diamond disk polishing down to 10 μm in thickness. Finally, they were made electron-transparent *via* PIPS ion polishing down to 60 nm in thickness or less. The parameters for this step, 2.5 keV ion energy and ±8° angle, were chosen to avoid sample damage.

The microstructure of the studied samples is shown in Fig. 1. The chosen implantation and annealing conditions lead in both cases to a dense system of bubbles. The bubbles are situated in a wide band, located between 200 and 400 nm from the sample surface. They can be classified in two groups: small bubbles making up the major part of the band, and large bubbles forming a line at its deepest edge. The different annealing temperatures yield different sizes and densities of bubbles, with greater diameters and fewer bubbles for the 700 °C samples than for the 500 °C samples. More specifically, after the 500 °C annealing, small bubbles are typically below 5 nm in diameter, while the larger ones exhibit a mean diameter of 10 nm. In 700 °C annealed samples, the bubble diameter is higher, typically

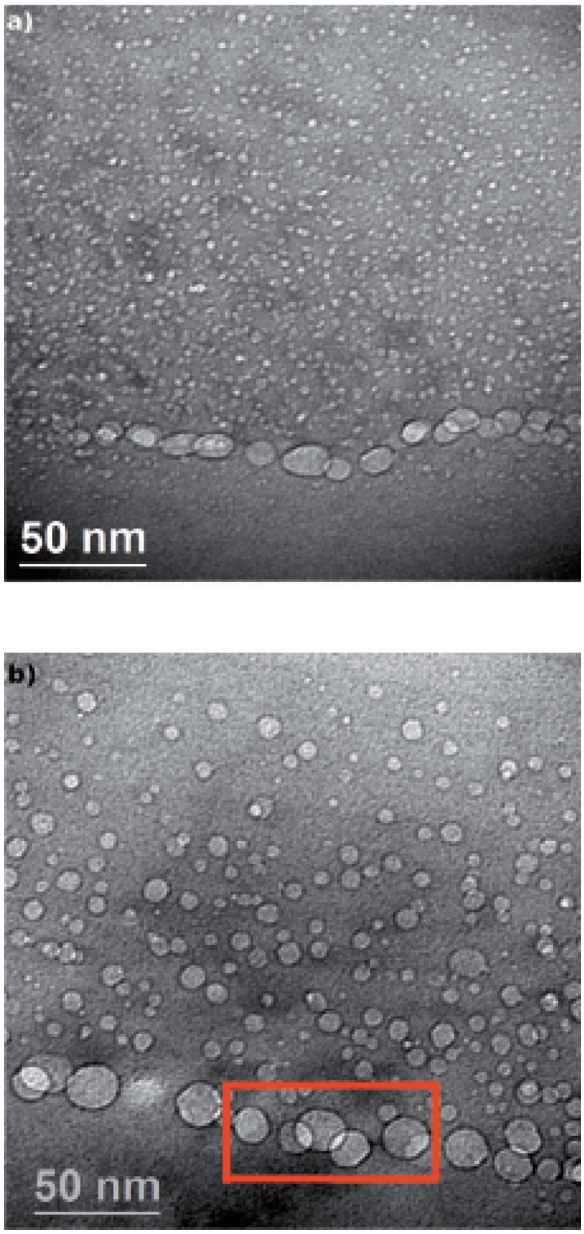

Fig. 1. Zero loss EFTEM images of Si samples implanted with 50 keV, 7.5×10^{16} cm^{-2} helium ions and annealed at (a) 500 °C and (b) 700 °C, filtered over the elastic peak with a 1 eV slit.

up to 10 nm for the smallest ones, while the largest ones can reach 20 nm in diameter. In this study we will mainly focus on bubbles exhibiting a diameter of 10 nm or more.

3. EFTEM helium density determination

3.1. Data acquisition

The microscope used for this study is a JEOL 2200FS with FEG operated at 200 keV, equipped with an in-column Ω filter and a Gatan Ultrascan 2048 × 2048 pixel CCD camera. Prior to data acquisition, the sample is oriented to minimize diffraction contrast in the observed area and an objective aperture is inserted giving a collection semi-angle for the spectrometer of 5.65 mrad. A nominal 100k× magnification, resulting in a final 200 nm × 200 nm field of view on the CCD, was chosen here in order to observe ten or more of the large bubbles simultaneously. Since helium densities are to

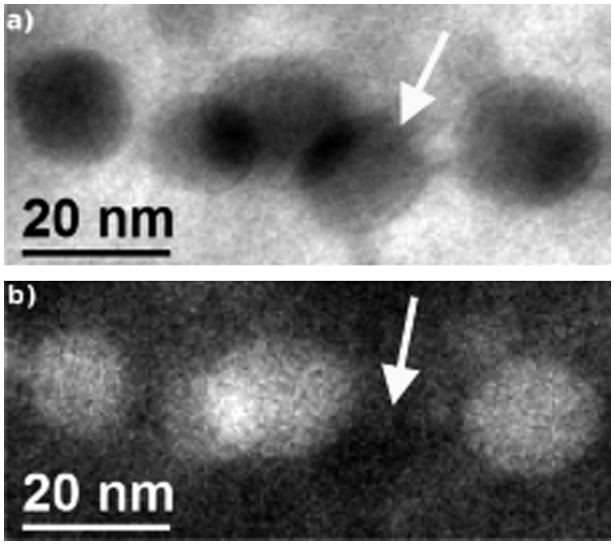

Fig. 2. EFTEM images acquired over (a) the Si plasmon and (b) the He K-edge, showing respectively the bubbles and which ones contain helium. (b) Shows that the bubble on the right of the central group marked by an arrow is empty.

be measured for individual bubbles, a requirement when picking observable areas is that bubble superposition has to be as limited as possible. Ideally, no superposition at all would be perfect, but in practice superposition at the edges is acceptable, on the condition that the central area of each bubble does not overlap with any part of another. In addition, one has to ensure that the chosen area includes mainly filled bubbles. During TEM sample preparation, some bubbles can be cut and emptied before observation, while still retaining their appearance in conventional TEM. Helium chemical mapping by EFTEM can be performed prior to datacube acquisition, to determine if an area with low superposition contains a majority of helium-filled bubbles. Fig. 2 shows images filtered on the Si plasmon and on the He-K edge of the area highlighted in Fig. 1a. As seen, five cavities are clearly evidenced either using underfocus conditions (Fig. 1a) or using the Si plasmon (Fig. 2a) but only four of them contain helium (Fig. 2b).

In the end, sample thickness is the parameter that determines the observability of an area: the probability of superposed bubbles increases with sample thickness, but the probability of empty ones decreases with it. We found that the ideal sample thickness is around twice the diameter of the largest bubbles, i.e. about 40 nm.

The 2200FS microscope accepts a minimal 0.2 eV step between acceleration energies for EFTEM, which on the spectra is equivalent to an 0.2 eV/channel dispersion. This is used to obtain the maximum amount of points when fitting the signal. The energy-selection slit has a lower limit of 0.5 eV, which will, for a perfect slit, integrate the post-filter signal with a boxcar function 0.5 eV wide, at each of the 0.2 eV steps. The smallest width is ideal to limit the convolution effects, and thus improve the resolution of the signal, however particles/dust and the wear effect of the electron beam on the slit itself over time create band-like artifacts across the image when performing EFTEM. Fig. 3 shows an example of stripes clearly visible around the elastic peak, while they are not observed around the Si plasmon for instance. This effect is detrimental to image quality in general, and can affect further processing (see Section 3.2.1) as it is not constant across the energy range. Cleaning or even changing the slit can reduce or remove the stripes. But one can try moving the stripes out of the observed area just by moving the slit slightly and changing the filter excitation. If the effect is still present, the remaining solution is to increase the slit width, thus decreasing the stripe contrast. This has the negative effect of increasing the resulting convolution width, but on the other hand improves the

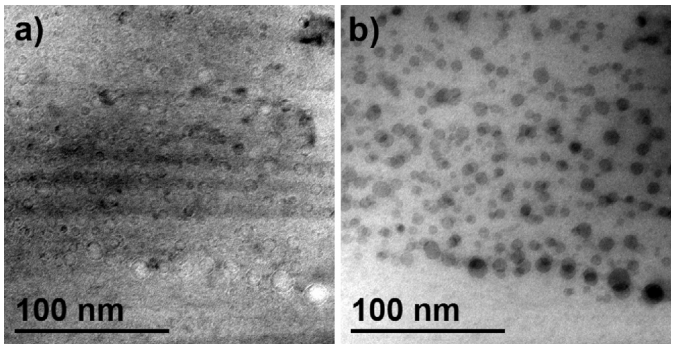

Fig. 3. (a) Stripes visible near the elastic peak with a 0.5 eV slit. (b) Absence of stripes on the Si plasmon with the same slit width.

signal/noise ratio. The results shown in this paper were obtained with a 1.0 eV slit, and 0.2 eV steps between each energy plane. However, upon further analysis, results obtained using 0.4 eV steps and an otherwise identical method, differed from 0.2 eV step results by less than the standard deviation of the measurements, thus demonstrating that the smallest 0.2 eV steps are not mandatory for accuracy. Increasing step sizes could also potentially help limit some of the issues described further.

For signal processing purpose, datacubes are acquired between −3 and 32 eV, encompassing the elastic peak and the expected Helium K-edge. During acquisition, the average intensity in the images will thus change drastically between elastic and inelastic parts of the spectrum. The spectrum in Fig. 4 depicts this variation, with an intensity ratio between the elastic peak and the Si plasmon of more than 20. Saturation or even damage must be prevented on the CCD camera, which is why the exposure must be tuned in relation to the maximum intensity. If the entire stack of energy filtered images is acquired with the same exposure time for every image, then the intensity of the elastic peak will lead to a poor signal/noise ratio even in the Si plasmon section. It is therefore necessary to change the exposure time during acquisition. The method used here simply divides the datacube in two, with a short (typically 0.5 s) exposure time for the elastic peak section and a longer one (generally ×10) for the Si plasmon and He K-edge section. The boundary between the two is usually set to 10 eV from the elastic peak, approximately. This reduces overall acquisition time, while increasing the signal to noise ratio on the He K-edge but also on the Si plasmon that might impact the deconvolution step of the analysis. A typical acquisition lasts 15 min.

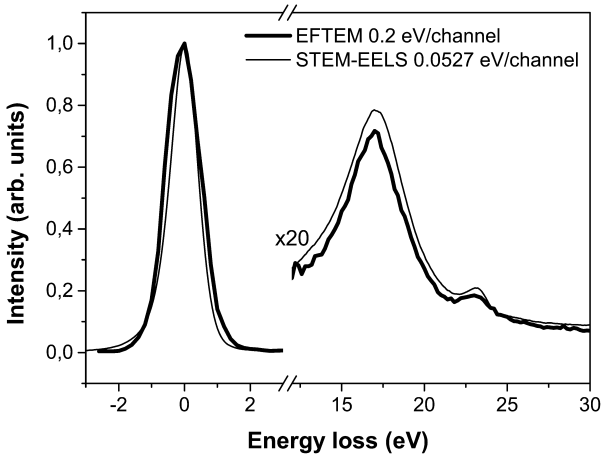

Fig. 4. Example averaged spectra from a full bubble, obtained via EFTEM-SI and STEM-EELS, and magnified (×20) to show the Si plasmon (17 eV) and He K-edge (22–24 eV).

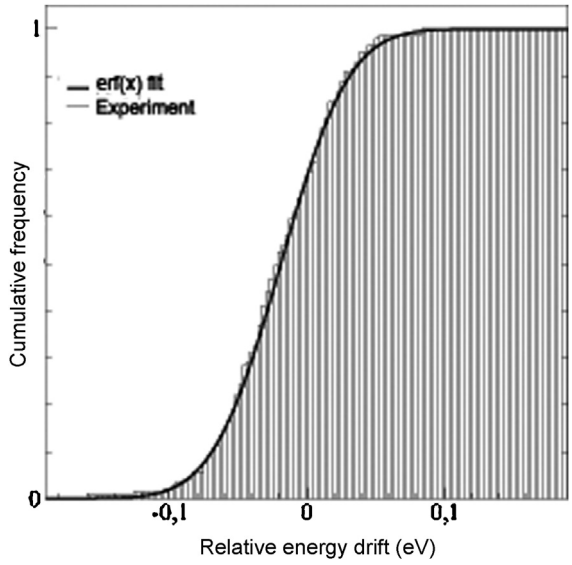

Fig. 5. Normalized cumulative histogram of energy drift and the erf(x) fit used to determine the parameters of the distribution.

Another important issue is spatial drift: the entire observed area can transit out of our 200 nm × 200 nm field of view during an acquisition. In a datacube, this means that each energy-filtered image is slightly spatially shifted relative to its neighbours. This translates to each spectrum being a blend of spectra from different points in space. This drift, due to its extent, prevents the study of bubbles whose diameters are 20 nm or less. Here, drift was limited by first respecting a waiting/stabilization period before each acquisition. However most of the time, additional manual compensation *via* piezo-electric movement has proven necessary during datacube acquisition. This manual compensation has to be restricted to the lapses of time during which the CCD is not acquiring an image (the user cannot see the sample moving). This procedure also limits data loss at the edges of the datacubes, thus maintaining a wide spatial area available for the analysis.

Besides the spatial drift, energy drift comes into play during acquisition. Observations show, in accordance with manufacturer specifications, that the mean energy of the elastically scattered electrons does vary at a pace that interferes with EFTEM as performed for this work. This means that the energy between consecutive planes is not constant over time and that an error or deviation has to be determined from energy-drift measurements.

Determining this deviation was done by repeatedly acquiring datacubes over the elastic peak only. In order to obtain a high enough sampling rate compared to the actual acquisition duration, acquisitions were made at a rate of one every minute and a half over periods of about 20 min. The datacubes ranged approximately from −3 to +3 eV around the initial position of the elastic peak. The acquisition conditions were otherwise the same as for full datacubes, out of sample, for clarity. This experiment was performed at different times of day, over a period of a few weeks, on a microscope whose tension was kept at 200 keV throughout. Spectra were extracted, fitted and relative energy drifts were determined. Assuming a Gaussian distribution of the relative energy drifts, the cumulative histogram was fitted with the error function, see Fig. 5, to determine the parameters of the distribution: mean energy drift and its standard deviation per periods of 90 s. Knowing the exposure time, by successive convolution the correction and error can be obtained between any two points on the energy-loss axis. Since this error and deviation increase with time, to improve the accuracy of the measurements the bulk Si plasmon has been chosen as the reference point, as it is the closest fixed feature to the helium K-edge on the spectra. Its position is measured for each individual datacube in an area empty of bubbles. The resulting energy drift error is the outcome of the successive convolutions of the energy drift distribution. The larger the energy between the reference and the He-K edge, the more convolutions will be needed and thus the larger the error. In this study, an experimental error of ±0.07 eV will be systematically used. This value has been calculated for a 24 eV He-K edge position, the highest energy position observed here. In addition, the correction for the measured mean variation (−0.0189 eV/90 s) will be performed for each datacube.

3.2. Data processing

Raw EFTEM datacubes require processing in order to extract the position of the He K-edge.

3.2.1. Realignment procedure

Two effects need to be corrected: spatial drift and non iso-chromaticity (NIC) (Schaffer et al., 2006). As mentioned in Section 3.1, spatial drift can be mitigated but not entirely cancelled. An additional step must therefore be taken to realign the slices as well as possible. NIC is related to the energy filter. When acquiring a filtered image, the energy of the electrons is not the same at every point of the CCD camera, and when acquiring a series of filtered images to obtain a datacube, the resulting spectra are shifted on the energy axis relative to one another. This might be corrected by fitting the elastic peak and shifting each spectra to match the others. While NIC and spatial drift can be corrected in a straightforward manner independently, their combination warps the ideal datacube in space and energy simultaneously. This requires a combined correction of those effects.

This procedure, largely inspired by (Schaffer et al., 2006), was coded in-house in order to adapt it as best as possible to our samples. The digital micrograph routine is available on demand (Note1). It consists of three steps to combine NIC and drift correction: first drift detection and NIC determination, then application of the spatial correction to both the original datacube and the NIC, and finally the energy correction of the spatially-corrected datacube with the spatially-corrected NIC, see Fig. 6.

The NIC map is determined by measuring the energy position of a known feature of the spectra at each spatial point of a datacube. Here, the elastic peak is used as such a feature. Once this first map is obtained, it is fitted with a third-order 2D polynomial to remove the noise, and this fit is used as the actual NIC map.

Before the drift detection takes place, a median and a Fourier filter are applied to the images. The purpose of the median filter (3 × 3 pixel size) is to remove the high intensity spikes from cosmic rays and some of the noise present on the filtered images. High and very low frequencies are then filtered, eliminating noise further as well as slow intensity variations across the image. The parameters are chosen to help with the next feature-detection step. The resulting filtered datacube is only used for drift detection: the original data are not modified yet.

The most straightforward approach to measuring drift is image cross correlation. Two images of a stack are cross-correlated, and the position of the maximum correlation gives the drift between the two. This method is most efficient when observing a moving object whose appearance remains the same for the duration of the observation. However, in the case of energy-filtered imaging, the images are bound to change with the energy. Around bubbles specifically, the contrast is inverted several times over the acquisition (see Fig. 2). However, while the contrast changes across the sample, its spatial repartition, linked to the bubbles, does not move independently. An adequate and versatile approach is therefore to detect drift by relying on contour or edge detection: a spatial-derivative function is applied to the images, and the resulting edges are cross

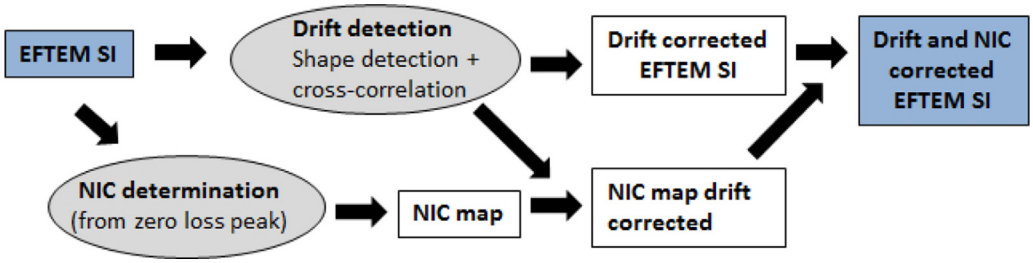

Fig. 6. Procedure used for the realignment of the datacubes, allowing for the spatial drift and non-isochromaticity (NIC) corrections.

correlated. In the case of bubbles, it is possible to go further with shape detection. All the bubbles being roughly circular, detecting the positions of circular objects in the images and correlating those positions allows to determine spatial drift. The parameters chosen in this work for the shape detection are focused on the larger bubbles, as they show the greatest contrast. The position of maximum correlation is theoretically used for the determination of the drift, as it is the point of best correlation. In practice, smoother results were achieved here by using a correlation-weighted average of the most correlated of those points, with a threshold set at 90% of the maximum. The result is a non-integer drift measurement, which can be more accurate as spatial drift is unlikely to precisely match pixel dimensions. This drift calculation is performed once for every image pair of the datacube, in order to obtain every possible drift value without choosing a particular reference frame. The combination of those correlation and drift values allows us to determine the drift for each image relative to all the others. If some image pairs have poor correlation, the corresponding values are calculated from intermediate image pairs with better correlation, in order to obtain usable drift values. By weighted averaging, the necessary drift compensation to be applied to the datacube is obtained. The procedure used here follows the work reported in Ref. Schaffer et al. (2004).

This method can leave some images uncompensated. Those that cannot be correlated to any others are usually feature-less, either because of a very poor signal/noise ratio in the concerned section of the spectrum, or inversely because the different components of the signal compensate one another, such that the filtered image appears uniform in intensity. Since there is no contrast that can be detected, moving the images does not change the result when extracting the spectrum, and therefore those images are placed at intermediate positions.

Once the compensation is obtained and applied to the original datacube, the combination step is necessary to adapt the NIC map to the now shifted images. This is done by creating a NIC datacube, within which the NIC map is copied and spatially shifted identically to the corresponding image for each energy plane. A final datacube is then created, and the drift-compensated points are moved to their correct energy planes according to the NIC datacube. Since it is nearly impossible that the energy shift matches exactly the 0.2 eV step between planes, the procedure involves filling the final points with Gaussian-weighted averages of the nearest shifted points. This is done along the energy axis only, and the weighting parameters are tuned to eliminate holes in the data, and limit residual non-isochromaticity and excessive spectrum smoothing.

Fig. 4 shows a typical spectrum that can be obtained in a bubble using the procedure described above. For comparison, a spectrum acquired using the STEM-EELS mode (raw data) in the conditions described in Ref. David et al. (2011) is also shown. As seen, despite a loss of resolution (1.3 eV in EFTEM against 1 eV in STEM-EELS measured as the full width at half maximum of the elastic peak) and a lower signal to noise ratio in EFTEM mode compared to what can be obtained with the same microscope in STEM-EELS mode, our experimental conditions and datacube realignment procedure produce a good He K-edge signal.

3.2.2. He peak extraction

Once the datacube has been corrected of experimental errors, the spectra are processed to eliminate noise, remove plural scattering and finally extract and fit the He K-edge. The steps of this procedure are shown in Fig. 7, and detailed in the following text. The IDL routine is available on request (Note1).

The first step to analyse the data is noise reduction. multivariate statistical analysis (MSA) is often the method of choice for spectral data analysis (Bonnet et al., 1999; Lucas et al., 2013), since it allows removal of noise but also extraction of the components of the signal that pertain to the composition of the sample. Unfortunately, noise reduction requires arbitrarily leaving only a reduced number of components to rebuild the dataset: while on a small dataset containing a single bubble this works well, on multiple bubbles there is a risk of smoothing the differences between them, since there is no spatial discrimination. The decision was therefore made to use a median filter on the filtered images, which combines the advantages of faster processing and reduced global averaging of the features of the signal, if a small enough pixel area is used for the filter. The signal obtained after this step is shown as a red curve in Fig. 7.

Multiple scattering is a common issue when dealing with spectra, even in relatively thin ($\leq$100 nm) samples. This is corrected by the Fourier Log method (Egerton, 2011), which, in the case of a perfectly noise-free signal, would result in the actual single-scattering signal obtained with a perfect electron gun (i.e. without energy spread). However, the noise remaining in the signal requires a reconvolution step, which leads, for the method applied here, to a single scattering-signal convolved with a Gaussian function (thick

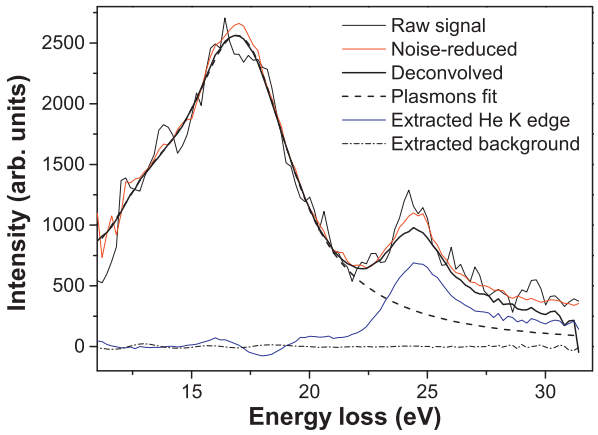

Fig. 7. Single spectrum extracted from a single full bubble (Si sample annealed at 500 °C), and the results from the successive He K-edge extraction steps. (For interpretation of the references to color in the text, the reader is referred to the web version of the article.)

black curve in Fig. 7). Its width is tuned to erase visible artifacts without flattening the signal excessively, which would red-shift the He K-edge.

In order to remove background signals, four features have to be fitted and substracted: the elastic peak, the bulk Si plasmon, the Si/SiO_2 interface plasmon, and the cavity plasmon. The cavity plasmon is fitted with a Gaussian function, while all the others are fitted with pseudo-Voigt functions which matched the signal better on our data. The elastic peak fit parameters (position, ratio and widths) are determined by an average of all the spectra in a datacube, while the amplitude is fitted spectrum by spectrum. It is fitted first, independently from the others. Afterward, the bulk Si plasmon and Si/SiO_2 interface plasmon are fitted in a similar fashion, except the average spectrum is extracted from a bubble-free area to eliminate artefacts introduced by the cavity plasmon. Once this first dual-plasmon fit is done, it is used as a base fit for all three plasmons, again spectrum by spectrum. Fitting two pseudo-Voigt functions and a Gaussian function simultaneously, i.e. 13 variables total, was initially attempted but rarely converged properly, which is why a fitting loop had to be implemented to override the automatic procedures along with the base-fit step. The fitting windows are tuned to limit negative intensities ahead of the He K-edge upon substraction of the ZLP and plasmons, specifically the Si plasmon fit window has to remain clear of the expected He K-edge. Here, a [10:19] eV window was used. The signal fit is shown as a black dashed curve in Fig. 7. Finally, in this work, a residual signal can be found across the entire datacube after substraction of the fits, situated close enough to the He K-edge to interfere with its measured position. This is assumed to be the combination of carbon contamination, SiO_2 plasmon and the remains of improperly fitted plasmons. It is removed by substracting an average sampled at multiple points where no bubbles are present, from all the spectra in the datacube. Finally, the extracted He K-edge (blue curve in Fig. 7) is fitted with a Gaussian to determine its position, taking as a reference the average position of the fitted Si plasmon. As seen in Fig. 7, dashed dot curve, the signal resulting from this procedure is nearly zero outside of the bubbles, as expected. This confirms the reliability of our He-K edge extraction procedure.

4. Helium density maps

Helium density n_{He} can be determined using the integrated intensity of the He K-edge (McGibbon, 1991; Walsh et al., 2000):

$$n_{He} = \frac{I_{He}}{I_{ZL}} \frac{1}{\sigma_{He} h} \quad (1)$$

where I_{ZL} and I_{He} are the integrated intensities of the elastic peak and the He K-edge (over 3 eV) respectively, σ_{He} is the cross-section for the $1s \rightarrow 2p$ excitation integrated over the collection angle and h is the thickness of the cavity crossed by the electron beam. In previous STEM-EELS experiments h bas been estimated as the complement to the local thickness measurements of the matrix (Taverna et al., 2008; David et al., 2011; Schierholz et al., 2015) or by measuring the bubble diameter on the high angle annular dark field image from intensity profiles if bubbles can be assumed to be spherical (Walsh et al., 2000; Frechard et al., 2009). With our setup, in the case of EFTEM measurements, it is difficult to record the energy loss over a sufficient energy range with a good signal/noise ratio to ensure a correct determination of the local thickness. Moreover, bubbles are not always spherical as it is clearly the case for the 500 °C annealed sample investigated in this study (see Fig. 1). Therefore, h cannot be determined with a sufficient accuracy and we had to use an alternative method.

Helium density can also be estimated using the blue shift of the helium K-edge (Rife et al., 1981; Lucas et al., 1983; David et al., 2011). The high density of helium contained in the bubbles tends to alter the electronic states energies by Pauli repulsion, leading to a shift in the corresponding EELS edges, which can be linked back to the density:

$$n_{He} = \frac{\Delta E}{C} \quad (2)$$

where $\Delta E = E - E_0$ is the helium K-edge shift as compared to its position for the free atom. In principle, this method provides a more direct determination of the helium density providing the constant of proportionality C is known with sufficient accuracy. In this study we use the value $C = 0.015$ at.nm^{-3} that we have determined in previous experiments for similar samples (David et al., 2011). Moreover, the position, E, of the helium K-edge is determined at the maximum of the extracted signal and the position for the free atom, E_0 is taken at 21.5 eV. This value is the smallest value we have determined from measurements in a bubble during *in situ* annealing experiments (Note2). This approach is slightly different from that which was previously applied in the literature, where a value $E_0^{abs} = 21.218$ eV (Kuhn, 1962) was systematically used. The latter is however only valid for a pure atomic absorption process, while the physical quantity measured by EELS is $Im[-1/\epsilon]$. In liquid helium, a red shift is observed between the maximum of the absorption part ϵ_2 of the dielectric function and the corresponding $Im[-1/\epsilon]$ (Lucas et al., 1983; Taverna, 2005; Surko et al., 1969). Using E_0^{abs} could thus lead to an over estimation of the helium density. Calculations are currently being performed to confirm a shift for higher helium density. Another issue is the systematic blue shift of the He K-edge coming from the instrumental energy resolution. This can be compensated by subtracting two values (E and E_0) measured using the same method.

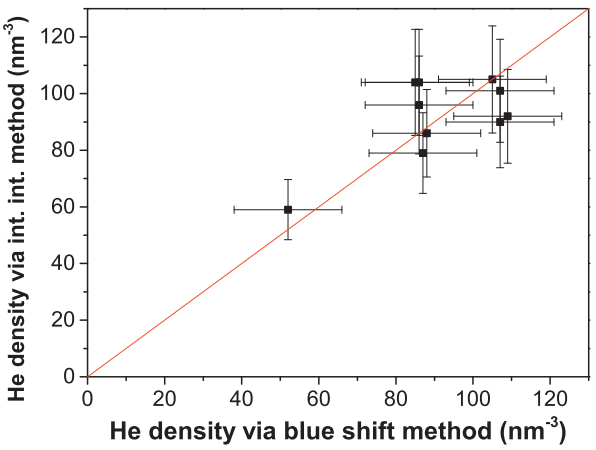

Fig. 8. Helium density measured using the integrated intensity method as a function of the helium density from the blue-shift method for ten bubbles of the Si sample annealed at 700 °C (see Fig. 1b). The red line shows the exact match between the two methods. (For interpretation of the references to color in this figure legend, the reader is referred to the web version of the article.)

Fig. 8 compares the helium density determined in ten of the bubbles of the sample annealed at 700 °C using both the integrated intensity and the blue-shift methods. These bubbles were chosen for their spherical aspects to ensure a correct determination of the thickness, h, crossed by the electron beam using the measurement of the bubble diameter. Bubbles in bright field conditions have to be imaged using either under or over focus conditions. An accurate determination of the bubble diameter being hardly feasible due to Fresnel finges, we have chosen to determine the bubble diameter by plotting intensity profiles from the image of the electronic density (image extracted from the datacube, filtered on the Si plasmon). As seen, both methods lead to very similar results, confirming the accuracy of our C value. Moreover, it is worth noticing that recently published experiments (Schierholz et al., 2015) are

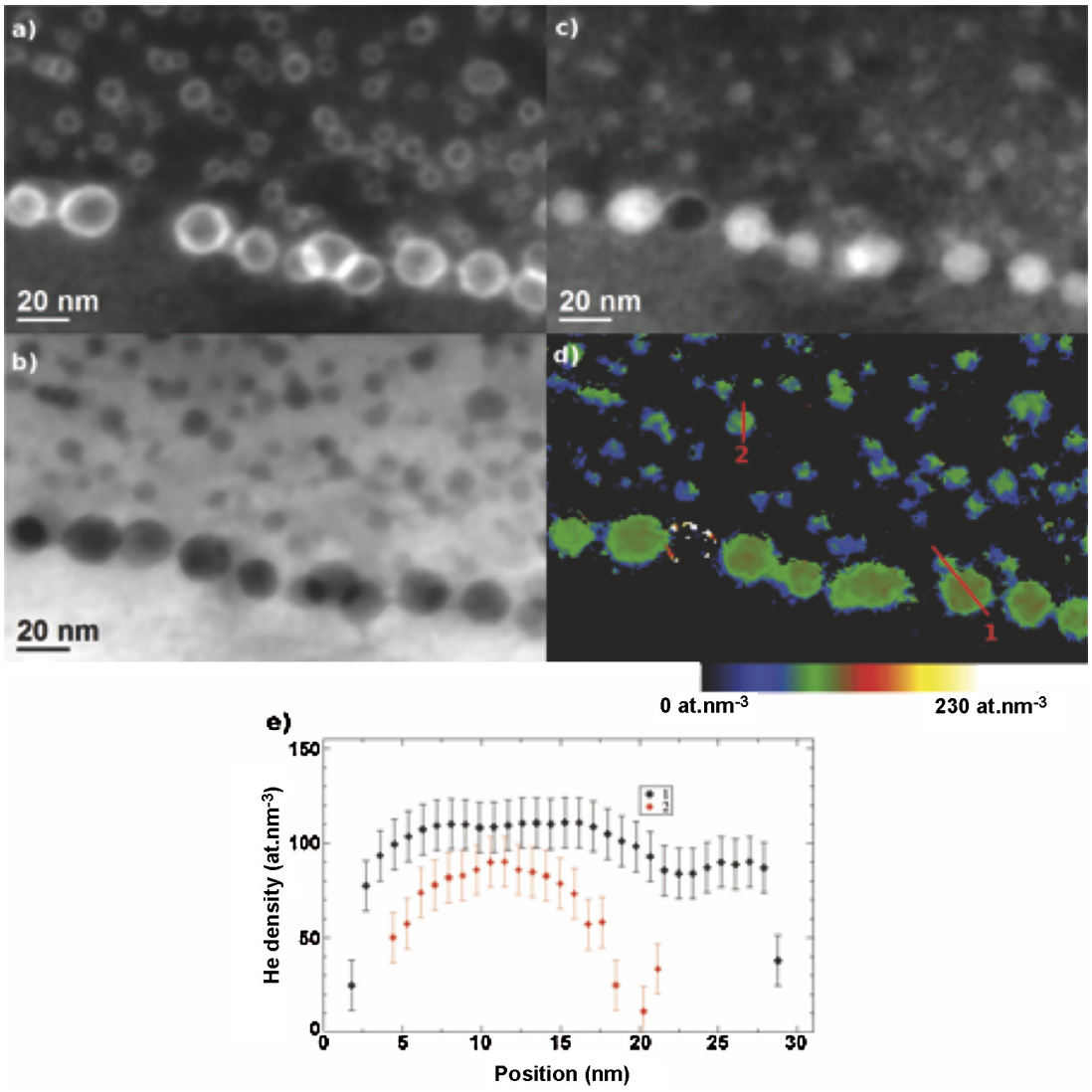

Fig. 9. Helium density map (d) obtained at room temperature for a sample annealed at 700 °C, and corresponding energy-filtered images for the cavity plasmon (a), Si plasmon (b) and He K-edge (c). (e) Shows two density profiles taken across the bubbles marked on (d).

in good agreement with this value. In addition, the points are well dispersed on both side of the diagonale (red line), indicating there is no systematic error.

The errors from the energy drift, and from the analysis itself are evaluated to a global 0.15 eV error on the measured He K-edge shift values. Each shift measurement is an average made at the center of each bubble over several pixels, leading to a standard deviation of 0.05 eV maximum in the data presented here. The global error is thus found to be 0.2 eV. Thus, the relative error amounts to 10% for a 2 eV shift and increases as the shift decreases. Therefore, as helium density decreases, measuring it accurately becomes more difficult. This is amplified by the difficulty of fitting the He K-edge when the helium density is small, since the intensity of the He K-edge is small as well, reducing the signal to noise ratio.

Fig. 9 shows energy-filtered images and helium density maps corresponding to the sample annealed at 700 °C previously shown in Fig. 1. As seen in Fig. 9a and b, the cavity and Si plasmon images allow clear localization of the bubbles, while the helium chemical map shows that most bubbles contain helium (Fig. 9c). Moreover, Fig. 9d shows that the density of all the large bubbles can be determined, as their localization and the presence of helium on the helium density map match the other images. In this sample, it has even been possible to partially determine the helium density in small bubbles as well. However, as could be expected, the smallest among those do not have enough pixels for statistically meaningful measurements. Note also that we have performed several successive measurements on the same area (and repeated the operation on other areas), and we have not observed any helium detrapping driven by the electron beam, contrary to STEM-EELS measurements. This shows that it is possible to determine with one datacube the helium density over a large number of bubbles at a time in a non destructive way.

As seen in Fig. 9d, the helium density is remarkably homogeneous across bubbles of similar diameter. The bubbles with diameters in the 20 nm size range (Fig. 9d) exhibit an helium density of 106 ± 15 at.nm^{-3}. This value is in close agreement with those determined in similar samples using a STEM-EELS approach (David et al., 2011, 2014). In bubbles of 10 nm or less, the helium density is smaller at 80 ± 15 at.nm^{-3}, which might seem in contradiction to usual findings. This bimodal distribution is probably due to the 700 °C thermal annealing, which allows equilibration of the helium contents among both populations of bubbles and/or helium desorption in the densest bubbles. Annealing at lower temperatures does not lead to a similar state. In fact, density measurements

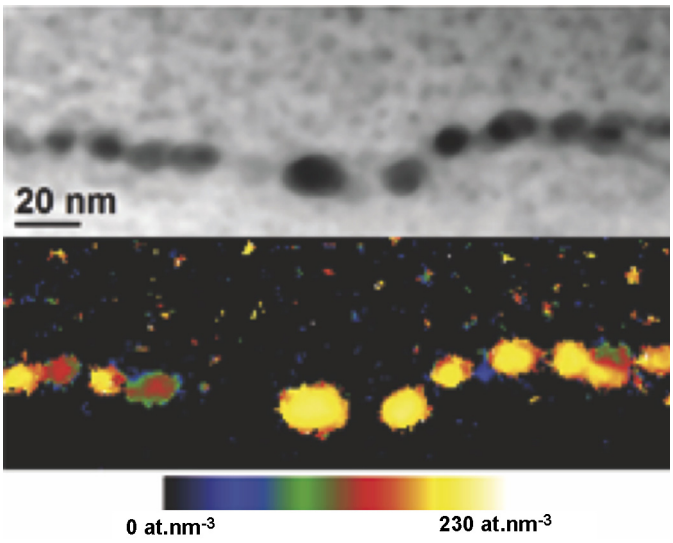

Fig. 10. Helium density map (b) obtained at room temperature for a Si sample annealed at 500 °C, and corresponding Si plasmon filtered image (a).

for the 500 °C annealed sample revealed largely inhomogeneous values (Fig. 10) for the largest bubbles, ranging from 100 ± 15 at.nm^{-3} to 190 ± 15 at.nm^{-3}. We clearly observe two different steps in the evolution of a condensed bubble layer under thermal annealing.

The density profiles in Fig. 9e also show that the measured helium density decreases in the vicinity of the bubble edges. This effect might be due to surface effects as reported in Ref. Taverna et al. (2008). Further investigations are needed to better understand this and to identify a way of correcting it.

5. Conclusion

We have developed a procedure allowing for the statistical determination of helium density in nanometer sized bubbles in silicon using energy-filtered transmission electron microscopy. Using this method for samples obtained by ion implantation and thermal annealing, the helium density in bubbles with sizes in the range 10–20 nm has been successfully measured in a non-destructive way. The accuracy of the density measurement is primarily related to the determination of the helium K-edge energy, which is estimated to be achieved with a 0.2 eV error. Assuming that the proportionality constant between the K-edge shift and the helium density is robust (David et al., 2011), this is the main error in the determination of the helium density in bubbles.

The measurement of helium density in nanometer sized bubbles has already been achieved in different materials using STEM-EELS (McGibbon, 1991; Walsh et al., 2000; Taverna et al., 2008; Frechard et al., 2009; David et al., 2011, 2014). Nevertheless, in the case of silicon, the electron beam was shown to lead to a concurrent detrapping of helium atoms from the bubbles (David et al., 2011, 2014). We show here that this effect can be suppressed using EFTEM-SI and the procedure described in this work, with a similar final accuracy. This will allow for successive measurements of the helium density in a given bubble, for instance in order to determine evolution mechanisms during *in situ* progressive annealing experiments.

Finally, we note that although the proposed procedure is developed for silicon, it can be adapted to other materials which might show similar detrapping in STEM-EELS. This opens the way to a versatile method for the complete determination of the state of helium-filled bubbles, an important step for achieving for a better understanding of irradiated materials in nuclear or microelectronics contexts.

Acknowledgement

K.A. acknowledges the French doctoral school SI-MMEA for financial support.

References

Agarwal, A., Haynes, T.E., Venezia, V.C., Holland, O.W., Eaglesham, D.J., 1998. Efficient production of silicon-on-insulator films by co-implantation of He+ with h+. Appl. Phys. Lett 72, 1086–1088.

Allen, F., Watanabe, M., Lee, Z., Balsara, N., Minor, A., 2011. Chemical mapping of a block copolymer electrolyte by low-loss {EFTEM} spectrum-imaging and principal component analysis. Ultramicroscopy 111 (3), 239–244 http://www.sciencedirect.com/science/article/pii/S0304399110003256

Bonnet, N., Brun, N., Colliex, C., 1999. Extracting information from sequences of spatially resolved EELS spectra using multivariate statistical analysis. Ultramicroscopy 77, 97–112.

Bruel, M., 1995. Silicon on insulator material technology. Electron. Lett. 31, 1201.

Cerofolini, G., Corni, F., Frabboni, S., Nobili, C., Ottaviani, G., Tonini, R., 2000. Hydrogen and helium bubbles in silicon. Mater. Sci. Eng. R: Rep. 27 (1–2), 1–52.

David, M.-L., Alix, K., Pailloux, F., Mauchamp, V., Couillard, M., Botton, G.A., Pizzagalli, L., 2014. In situ controlled modification of the helium density in single helium-filled nanobubbles. J. Appl. Phys. 115 (12) http://scitation.aip.org/content/aip/journal/jap/115/12/10.1063/1.4869213

David, M.-L., Pailloux, F., Mauchamp, V., Pizzagalli, L., 2011. In situ probing of helium desorption from individual nanobubbles under electron irradiation. Appl. Phys. Lett. 98 (17), 171903.

Donnelly, S., Evans, J., 1991. Fundamental Aspects of Inert Gases in Solids. Plenum Press, New York.

Egerton, R., 2011. Electron Energy-Loss Spectroscopy in the Electron Microscope. Springer, New York.

Eggeman, A.S., Dobson, P.J., Petford-Long, A.K., 2007. Optical spectroscopy and energy-filtered transmission electron microscopy of surface plasmons in core–shell nanoparticles. J. Appl. Phys. 101 (2), 024307 http://scitation.aip.org/content/aip/journal/jap/101/2/10.1063/1.2424404

Frechard, S., Walls, M., Kociak, M., Chevalier, J., Henry, J., Gorse, D., 2009. Study by EELS of helium bubbles in a martensitic steel. J. Nucl. Mater. 393 (1), 102–107.

Godinho, V., Caballero-Hernandez, J., Jamon, D., Rojas, T.C., Schierholz, R., Garcia-Lopez, J., Ferrer, F.J., Fernandez, A., 2013. A new bottom-up methodology to produce a silicon layers with a closed porosity nanostructure and reduced refractive index. Nanotechnology 24 (27), 275604 http://stacks.iop.org/0957-4484/24/i=27/a=275604

Guilbert, S., Sauvage, T., Erramli, H., Barthe, M.-F., Desgardin, P., Blondiaux, G., Corbel, C., Piron, J., 2003. Helium behavior in {UO2} polycrystalline disks. J. Nucl. Mater. 321 (2–3), 121–128 http://www.sciencedirect.com/science/article/pii/S0022311503002125

Iyyakkunnel, S., Marot, L., Eren, B., Steiner, R., Moser, L., Mathys, D., Dggelin, M., Chapon, P., Meyer, E., 2014. Morphological changes of tungsten surfaces by low-flux helium plasma treatment and helium incorporation via magnetron sputtering. ACS Appl. Mater. Interfaces 6 (14), 11609–11616, http://dx.doi.org/10.1021/am502370t, pMID:24960311.

Jaeger, W., Manzke, R., Trinkaus, H., Crecelius, G., Zeller, R., Fink, J., Bay, H., 1982. Density and pressure of helium in small bubbles in metals. J. Nucl. Mater. 111–112, 674–680 http://www.sciencedirect.com/science/article/pii/0022311582902884

Jaeger, W., Manzke, R., Trinkaus, H., Zeller, R., Fink, J., Crecelius, G., 1983. The density and pressure of helium in bubbles in metals. Radiat. Effects 78 (1–4), 315–325.

Jeanguillaume, C., Colliex, C., 1989. Spectrum-image: the next step in {EELS} digital acquisition and processing. Ultramicroscopy 28 (1–4), 252–257 http://www.sciencedirect.com/science/article/pii/0304399189903045

Kajita, S., Yoshida, T., Kitaoka, D., Etoh, R., Yajima, M., Ohno, N., Yoshida, H., Yoshida, N., Terao, Y., 2013. Helium plasma implantation on metals: nanostructure formation and visible-light photocatalytic response. J. Appl. Phys. 113 (13), 134301 http://scitation.aip.org/content/aip/journal/jap/113/13/10.1063/1.4798597

Kuhn, H.G., 1962. Atomic Spectra, 132.

Lavergne, J.-L., Martin, J.-M., Belin, M., 1992. Interactive electron energy-loss elemental mapping by the "imaging-spectrum" method. Microsc. Microanal. Microstruct. 3 (6), 517–528, http://dx.doi.org/10.1051/mmm:0199200306051700

Lucas, A.A., Vigneron, J.P., Donnelly, S.E., Rife, J.C., 1983. Theoretical interpretation of the vacuum ultraviolet reflectance of liquid helium and of the absorption spectra of helium microbubbles in aluminum. Phys. Rev. B 28 (September), 2485–2496.

Lucas, G., Burdet, P., Cantoni, M., Hébert, C., 2013. Multivariate statistical analysis as a tool for the segmentation of 3d spectral data. Micron 52–53, 49–56 http://www.sciencedirect.com/science/article/pii/S0968432813001261

Manzke, R., Jaeger, W., Trinkaus, H., Crecelius, G., Zeller, R., Fink, J., 1982. Quantitative determination of the pressure of He in bubbles in Al and Ni. Solid State Commun. 44 (4), 481–484 http://www.sciencedirect.com/science/article/pii/0038109882901284

McGibbon, A.,1991. Application of peels on a stem to the problem of inert gas bubbles in solids. In: Proceedings of the Institute of Physics Electron Microscopy and Analysis Group Conference. Vol. 119 of Institute of Physics Conference. IOP Publishing, pp. 109–112.

Nelayah, J., Gu, L., Sigle, W., Koch, C.T., Pastoriza-Santos, I., Liz-Marzán, L.M., van Aken, P.A., 2009 Apr. Direct imaging of surface plasmon resonances on single triangular silver nanoprisms at optical wavelength using low-loss EFTEM imaging. Opt. Lett. 34 (7), 1003–1005 http://ol.osa.org/abstract.cfm?URI=ol-34-7-1003

Note1, Send an email to marie-laure.david@univ-poitiers.fr.

Note2, Bubbles were emptied step by step during in situ annealing experiments and at each step, the position of the He K-edge was determined. E0 was determined as the convergence value of the exponential fit on these data. These results will be published elsewhere.

Petersen, G., Myers, S., Follstaedt, D., 1997. Nucl. Inst. Methods Phys. Res. B 127/128, 301.

Raineri, V., Saggio, M.E.R., 2000. Voids in silicon by he implantation: from basic to applications. J. Mater. Res. 15, 1449–1477.

Rife, J.C., Donnelly, S.E., Lucas, A.A., Gilles, J.M., Ritsko, J.J., 1981. Optical absorption and electron-energy-loss spectra of helium microbubbles in aluminum. Phys. Rev. Lett. 46 (May), 1220–1223, http://dx.doi.org/10.1103/PhysRevLett.46.1220

Schaffer, B., Grogger, W., Kothleitner, G., 2004. Automated spatial drift correction for EFTEM image series. Ultramicroscopy 102 (1), 27–36.

Schaffer, B., Grogger, W., Kothleitner, G., Hofer, F., 2010. Comparison of {EFTEM} and {STEM} {EELS} plasmon imaging of gold nanoparticles in a monochromated {TEM}. Ultramicroscopy 110 (8), 1087–1093 http://www.sciencedirect.com/science/article/pii/S0304399109002903

Schaffer, B., Kothleitner, G., Grogger, W., 2006. EFTEM spectrum imaging at high-energy resolution. Ultramicroscopy 106, 1129–1138.

Schaffer, B., Riegler, K., Kothleitner, G., Grogger, W., Hofer, F., 2009. Monochromated, spatially resolved electron energy-loss spectroscopic measurements of gold nanoparticles in the plasmon range. Micron 40 (2), 269–273 http://www.sciencedirect.com/science/article/pii/S0968432808001637

Schierholz, R., Lacroix, B., Godinho, V., Caballero-Hernandez, J., Duchamp, M., Fernandez, A., 2015. STEM-EELS analysis reveals stable high-density He in nanopores of amorphous silicon coatings deposited by magnetron sputtering. Nanotechnology 26 (7), 075703 http://stacks.iop.org/0957-4484/26/i=7/a=075703

Sigle, W., Nelayah, J., Koch, C., Ögüt, B., Gu, L., van Aken, P., 2010. {EFTEM} study of surface plasmon resonances in silver nanoholes. Ultramicroscopy 110 (8), 1094–1100 http://www.sciencedirect.com/science/article/pii/S0304399110000872

Sugar, J.D., Gabaly, F.E., Chueh, W.C., Fenton, K.R., Tyliszczak, T., Kotula, P.G., Bartelt, N.C., 2014. High resolution chemical analysis on cycled LiFePo4 battery electrodes using energy-filtered transmission electron microscopy. J. Power Sources 246, 512–521 http://www.sciencedirect.com/science/article/pii/S0378775313013402

Surko, C.M., Dick, G.J., Reif, F., Walker, W.C., 1969. Spectroscopic study of liquid helium in the vacuum ultraviolet. Phys. Rev. Lett. 23 (October), 842–846, http://dx.doi.org/10.1103/PhysRevLett. 23.842

Taverna, D., (Ph.D. thesis) 2005. Excitations électroniques de nano-objets individuels, analyses par sepctroscopie de pertes d'énergie d'électrons á haute résolution spatiale. Université Paris XI.

Taverna, D., Kociak, M., Stéphan, O., Fabre, A., Finot, E., Décamps, B., Colliex, C., 2008. Probing physical properties of confined fluids within individual nanobubbles. Phys. Rev. Lett. 100 (January), 035301.

Tillmann, K., Hüging, N., Trinkaus, H., Luysberg, M., 2004. Quantitative transmission electron microscopy analysis of the pressure of helium-filled cracks in implanted silicon. Microsc. Microanal. 10, 199–214 http://journals.cambridge.org/article_S1431927604040024

Trinkaus, H., 1983. Energetics and formation kinetics of helium bubbles in metals. Radiat. Effects 78 (1–4), 189–211, http://dx.doi.org/10.1080/00337578308207371

Trinkaus, H., Singh, B.N., 2003. Helium accumulation in metals during irradiation – where do we stand ? J. Nucl. Mater. 323, 229–242.

Verbeeck, J., Dyck, D.V., Tendeloo, G.V., 2004. Energy-filtered transmission electron microscopy: an overview. Spectrochim. Acta B: At. Spectrosc. 59 (10–11), 1529–1534, 17th International Congress on X-Ray Optics and Microanalysis.

Walsh, C.A., Yuan, J., Brown, L.M., 2000. A procedure for measuring the helium density and pressure in nanometre-sized bubbles in irradiated materials using electron-energy-loss spectroscopy. Philos. Mag. A 80 (7), 1507–1543.